



New Composite Nanomaterials with Antimicrobial and Photocatalytic Properties Based on Silver and Zinc Oxide

Anca Dumbrava¹ · Daniela Berger² · Cristian Matei² · Gabriel Prodan³ · Florin Aonofriesei⁴ · Marius Daniel Radu⁴ · Florin Moscalu⁵

Received: 2 March 2019 / Accepted: 20 April 2019 / Published online: 30 April 2019
© Springer Science+Business Media, LLC, part of Springer Nature 2019

Abstract

Herein we report the synthesis of composites containing nanobio silver, ZnO and phytochemicals in different Ag/Zn molar ratios. First, Ag nanoparticles were prepared using red cabbage extract and then they are covered with zinc oxide obtained also in the same extract by precipitation method. The antimicrobial activity of synthesized nanocomposites was tested against *Staphylococcus aureus*, *Streptococcus*, *Escherichia coli*, *Pseudomonas* and *Candida* clinical isolates and compared with that of ZnO functionalized with anthocyanins. The presence of nanobio silver into the nanocomposites enhanced the bactericidal properties demonstrated by slightly larger diameters of growth inhibition zone and lower minimal inhibitory concentrations. *S. aureus* and *Streptococcus* strains were more sensitive than the other strains and fungi both for Ag–ZnO nanocomposites and ZnO functionalized with anthocyanins. Also, the presence of silver in the nanocomposites leads to an improved photocatalytic activity (PA) confirmed in the bleaching of Congo red solution. The PA increases with silver content when Ag content is low (up to 1/12 Ag/Zn molar ratio), but decreases significantly for high silver concentration (1/7 Ag/ZnO molar ratio) in the Ag–ZnO nanocomposites.

Keywords Ag–ZnO nanocomposites · Biosynthetic method · Nanobio silver · Photocatalytic activity · Antimicrobial activity

Electronic supplementary material The online version of this article (<https://doi.org/10.1007/s10904-019-01166-4>) contains supplementary material, which is available to authorized users.

✉ Anca Dumbrava
adumbrava@univ-ovidius.ro

- ¹ Department of Chemistry and Chemical Engineering, Ovidius University of Constanta, Constanta, Romania
- ² Department of Inorganic Chemistry, Physical Chemistry and Electrochemistry, University Politehnica of Bucharest, Bucharest, Romania
- ³ Electron Microscopy Laboratory, Ovidius University of Constanta, Constanta, Romania
- ⁴ Faculty of Natural and Agricultural Sciences, Ovidius University of Constanta, Constanta, Romania
- ⁵ Department of Physics, Ovidius University of Constanta, Constanta, Romania

1 Introduction

The synthesis of silver nanoparticles in vegetal extracts (“nanobio silver”) is one of the most reliable applications of biotechnology in the inorganic nanomaterials domain [1–3]. This kind of synthesis, in which are used natural compounds acting both as reducing and stabilizing agents, is a bottom-up approach that leads to nanoparticles with lower toxicity and enhanced biocompatibility [2].

The interest for Ag nanoparticles is related to their applications in medicine, electronics, catalysis, as optical biosensors, etc. Among these, the biomedical ones are probably better studied because of Ag nanoparticles anti-inflammatory, antitumor, antiviral, antibacterial, and wound healing features [4]. Especially for water treatment and therapeutic uses, the silver synthesis medium is very important. So, the phytochemical synthesis of silver nanoparticles, which generates non-toxic products, is often preferred in the case of therapeutic applications being the best option for the large scale preparation [1, 3, 4].

Nanobio silver was obtained using various vegetal extracts, e.g. leaves of *Alstonia scholaris* [5], flowers of *Osmanthus fragrans* [6], seeds of *Artocarpus heterophyllus* Lam. [7], fruits of black elderberry [4], marine red alga *Laurencia catarinensis* [8], etc. Several vegetables from *Brassicaceae* family, known for their antioxidant, antimicrobial, anticancer and antifungal properties, were also used for Ag nanoparticles synthesis [1, 7, 9, 10]. Due to their reducing properties, the phytochemicals can act as reducing agents for Ag(I), but they can also act as capping agents avoiding silver nanoparticles aggregation, which considerably affects their chemical and antibacterial properties [11].

Another approach to hamper the Ag nanoparticles aggregation is to cover them with a layer of metal oxide (ZnO, MgO, CaO), the core–shell morphology offering a large surface to volume ratio [11]. The composites containing noble metals and metal oxides are of interest for applications like drug delivery, photocatalysis, solar cells, etc. and their properties are influenced by their structure and morphology [12].

Zinc oxide was also obtained in a wide variety of vegetal extracts and unlike metal nanoparticles, in this case the phytochemicals act only as template and capping agents. Thus, various shapes of ZnO nanoparticles were obtained by changing the natural compounds [13, 14] and during the synthesis the vegetal pigments can bind to the ZnO nanoparticles surface forming colored ZnO nanopowders [15].

Several reports highlighted for Ag–ZnO composites, synthesized by varied routes (sol–gel, hydrothermal, photochemical, etc.), gas sensing, optical, antimicrobial and photocatalytic properties [16–19]. The antibacterial activity and its mechanism were also described [11, 20, 21] and a synergistic antibacterial effect of this kind of nanocomposites was demonstrated [18].

Herein we report the synthesis of anthocyanins capped Ag–ZnO nanocomposites with different Ag/Zn molar ratios containing Ag nanoparticles prepared by reduction of Ag(I) in aqueous red cabbage extract (RCE), followed by their covering with blue ZnO obtained by chemical precipitation in the same extract. The antimicrobial properties of nanocomposites were assessed against bacteria and fungi. Also, their photocatalytic properties were tested in the degradation of Congo red (CR) azo dye.

2 Experimental

2.1 Materials

The reagents of high purity were obtained from Sigma-Aldrich (silver nitrate, AgNO₃; zinc acetate, Zn(CH₃COO)₂·2H₂O; methanol 99.8%, CH₃OH; CR) and Loba Chemie (sodium hydroxide, NaOH), and were used as received, without further purification. CR (C.I. Direct Red

28, MW = 696.67 g/mol, C₃₂H₂₄N₆O₆S₂Na₂) is the disodium salt of 3,3'-([1,1'-biphenyl]-4,4'-diyl)bis(4-aminonaphthalene-1-sulfonic acid). Red cabbage (*Brassica oleraceae*) was purchased from Romanian local market.

Antimicrobial activity of powders was investigated using bacterial strains (*Staphylococcus*—hemolytic, isolated from ocular infection and ocular secretions, *Streptococcus*—beta-hemolytic, isolated from throat infection, *Escherichia coli* isolated from urinary tract infection, *Pseudomonas* isolated from ear secretions), and *Candida* strains (*Candida albicans* isolated from throat and mouth infection).

2.2 Synthesis of Ag–ZnO Nanocomposites

The red cabbage leaves were washed with distilled water and dried. On 100 g of small pieces of red cabbage leaves were added 200 mL of distilled water and kept in a microwave oven (Merck Microwave Oven) for 5 min at 1000 W. The hot resulted mixture was filtered through a cotton pad and a purple solution was obtained (RCE).

Different quantities of AgNO₃—i.e. 0.0255 g (0.15 mmol) for Ag–ZnO **1**, 0.034 g (0.2 mmol) for Ag–ZnO **2**, 0.051 g (0.3 mmol) for Ag–ZnO **3**, and 0.51 g (3 mmol) for Ag–ZnO **4**, were dissolved in 50 mL of RCE and the resulted solutions were magnetically stirred for 1 h, at 60 °C. In all cases a dark brown colloidal solution was obtained.

Four solutions resulted by dissolving each 6.6 g Zn(CH₃COO)₂·2H₂O (30 mmol) in 50 mL RCE were mixed with the Ag colloidal solutions, under magnetic stirring at room temperature. After 15 min of stirring, a 1 M NaOH aqueous solution was added drop by drop in each mixture, till pH 8. Further, the mixtures were heated at 80 °C, under magnetic stirring, for 2 h. The blue-gray powders (Ag–ZnO **1**, Ag–ZnO **2**, Ag–ZnO **3**), respective the dark brown one (Ag–ZnO **4**) were filtered off, washed with water, and dried in air at room temperature.

For comparison, we also synthesized ZnO functionalized with anthocyanins, by one-pot precipitation method, in the RCE, at pH 8, using a slightly modified published procedure [15].

2.3 Characterization of Nanocomposites

The synthesized nanocomposites were investigated by X-ray diffraction (XRD) performed on a Rigaku Miniflex 2 diffractometer with Ni filtered Cu K α radiation, in the range of 20°–70° 2 θ , scan rate of 2°/min and a step of 0.02°. The morphology of powders was analyzed using a Tescan Vega 3LMH scanning electron microscope (SEM), equipped with a back-scattered electron (BSE) detector. In order to identify the materials composition, energy dispersive X-ray spectroscopy (EDX) analysis was performed on the SEM equipped with a Bruker X-ray energy dispersive detector.

The investigation by transmission electron microscopy (TEM) was performed on a Philips CM 120 ST transmission electron microscope operated at 100 kV, with 2 Å resolution. The FTIR spectra were recorded on a Bruker Tensor 27 spectrometer using KBr pellets technique, in the wave number range of 400–4000 cm⁻¹. The UV–visible diffuse reflectance spectra were recorded in the range of 220–850 nm, on a Jasco V 550 spectrophotometer with an integrating sphere using MgO as the reference. The same spectrophotometer was also used for performing UV–visible spectra of solutions (200–900 nm).

2.4 Antimicrobial Activity

The antimicrobial activity of nanocomposites containing nanobio silver, ZnO and phytochemicals was estimated by the disk diffusion method [22]. Bacterial strains were grown on Trypticase soy broth (TSB, Fisher Scientific) for 16–24 h. *Candida* strains were grown on Sabouraud dextrose broth (SDB, Lab M) for 16–24 h. The bacterial strains were inoculated by spreading overnight culture on Muller Hinton agar (MHA, Thermo Scientific). Thereafter, wells (d = 9 mm) were performed on MHA by using a sterile test tube. The same procedure was used for *Candida* and diffusion test was performed on Sabouraud dextrose agar (Lab M). The powders were dispersed (1 g/L) in a solution of methanol in water (20% v/v) and 100 µL of each sample were pipetted into wells. Inoculated plates were kept at room temperature for 1 h to allow the diffusion of nanoparticles. Subsequently, plates were incubated at 37 °C for 48 h. The width of inhibition zone was measured after the incubation period.

The minimal inhibitory concentration (MIC) was estimated by macrodilution broth method [23–25]. Serial dilutions of each sample were prepared in TSB for bacterial strains and in SDB for *Candida* strains with concentration ranging from 5 to 320 µg/mL. 10 µL of cell suspensions (with density between 2 × 10⁵ and 2 × 10⁶ CFU/mL) were inoculated in test-tubes containing TSB (for bacterial strains) and SDB (for *Candida* strain) and increasing concentrations of each sample. The test tubes were incubated at 37 °C and MIC was determined after examination of turbidity as the highest concentration of sample without visible growth. All biological experiments were performed in triplicates.

2.5 Photocatalytic Activity

The photocatalytic properties were tested in the degradation of CR azo dye. The photocatalytic experiments were performed following the procedure published in our previous papers [26, 27], by using a halogen lamp of 45 W. The maximum of absorption for initial CR solution was identified at 497 nm. The photodegradation was estimated by C_t/C_0 ratio (where C_t and C_0 are the concentrations of CR at

certain time, t , and initial concentration, respectively). The efficiency of nanocomposites as photocatalysts was evaluated by the photocatalytic activity (PA):

$$PA = \frac{C_0 - C_t}{C_0} \times 100 = \frac{A_0 - A_t}{A_0} \times 100, \quad (1)$$

where A_0 , A_t are the absorbance value for CR solutions when the reaction time is 0 and t , respectively (based on Lambert–Beer law) [27].

3 Results and Discussion

3.1 Characterization of Nanocomposites

The crystalline phases were identified by XRD (Fig. 1).

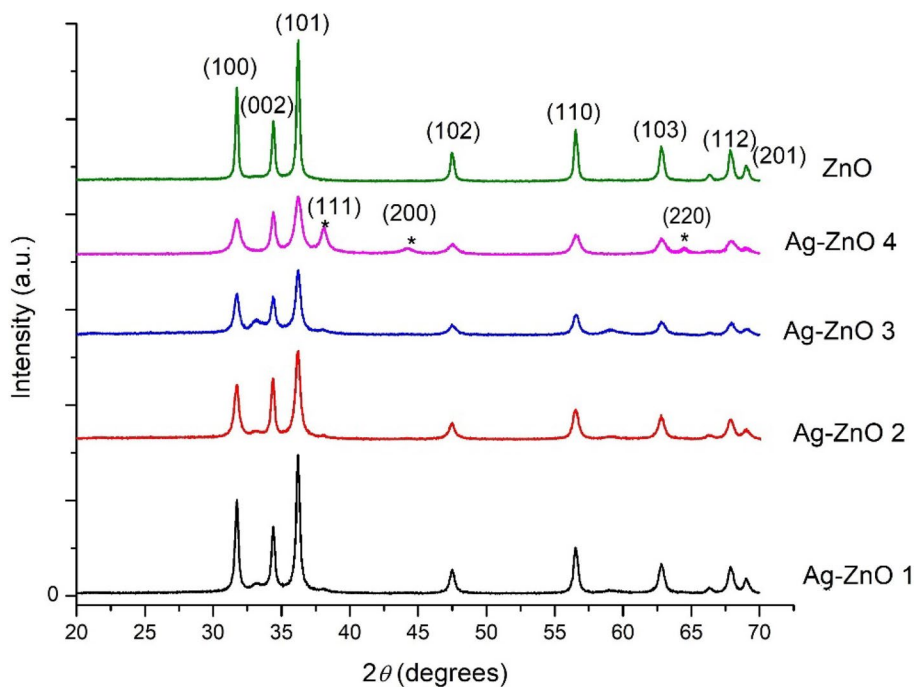
Zinc oxide crystallized in the hexagonal wurtzite structure (JCPDS 36-1451) was evidenced in all analyzed samples [18, 28]. The crystallite size for ZnO particles has been determined from the XRD data using Rigaku PDXL software based on Scherrer's equation [29] from (1 0 1) diffraction Bragg reflection. The calculated values are 31 nm (Ag–ZnO 1), 24 nm (Ag–ZnO 2), 22 nm (Ag–ZnO 3), and 16 nm (Ag–ZnO 4). It is interesting to remark that all values are smaller compared to ZnO crystallite size (40 nm) and decrease with the Ag content.

The synthesis of Ag nanoparticles is confirmed by the diffraction peaks at 38.116° (1 1 1), 44.277° (2 0 0), and 64.426° (2 2 0), characteristic for cubic silver (JCPDS 04-0783), which intensity increases from Ag–ZnO 1 to Ag–ZnO 4, with the Ag content [30]. A peak with low intensity, positioned around 33.5°, can be observed for Ag–ZnO 1, Ag–ZnO 2, and Ag–ZnO 3 samples. This peak results as an overlap between two peaks, i.e. at 33.30° (1 1 1) and 34.13° (3 0 0), which are characteristic for Ag₂CO₃ phase (JCPDS 31-1237). By increasing the Ag content, this peak has disappeared. The synthesis of silver compounds during the Ag nanoparticles biosynthesis was also reported by other authors [31].

The morphology of nanopowders was revealed by SEM investigation. The SEM images obtained via BSEs detector illustrate the agglomeration of ZnO nanoparticles around the Ag nanoparticles (Fig. 2). The resulted agglomerations are in the range of 100–400 nm, as it was estimated from SEM micrographs (Supplementary material).

The Ag/Zn molar ratios were calculated from EDX data (Table 1). Their values are superior to the reagents' ratio, demonstrating a higher yield for Ag nanoparticles synthesis in comparison with ZnO formation. The identification of a low silver content by XRD can be due to the presence of Ag(I) compounds (i.e. Ag₂CO₃) both in amorphous and crystalline phases.

Fig. 1 XRD patterns for synthesized samples (the unmarked peaks are assigned to ZnO and the peaks marked with asterisk are assigned to Ag)



The TEM images confirm the agglomeration of nanoparticles in bigger aggregates, consisting in flake-like ZnO nanoparticles clustered probably around Ag nanoparticles, as it is illustrated for Ag–ZnO **3** sample (Fig. 3). The flake-like shape for anthocyanins functionalized ZnO nanoparticles was also identified in a previous study, in absence of Ag [15]. However, for higher Ag concentration, TEM images revealed a different morphology, with smaller ZnO aggregates decorated with Ag nanoparticles (Fig. 3).

The synthesis of Ag nanoparticles was noticed by the change of RCE color. The intense color of the silver nanoparticles dispersions is due to the plasmon resonance absorption, which is influenced by the particles size and shape [32].

The color change in time was evidenced by UV–vis spectroscopy. The fast disappearance of the band assigned to anthocyanins from 553 nm and the occurrence of a new and intense band at 442 nm, and then at 452 nm can be seen in UV–vis spectra (Fig. 4a). The intensity and position of band assigned to Ag are dependent on the quantity and dimension of nanoparticles, moving to higher wavenumbers with increasing size [32, 33].

In addition to the usual phytochemicals in a vegetal extract, including the biopolymers which can act as a template, the presence of anthocyanins, with remarkable antioxidative properties, is an advantage for the silver synthesis in the RCE. Furthermore, the color of nanocomposites is influenced by the anthocyanins. The optical properties of Ag–ZnO nanocomposites were studied by UV–vis diffuse reflectance spectroscopy.

The electronic spectra of Ag–ZnO **1**, Ag–ZnO **2**, and Ag–ZnO **3** are quite similar with that of ZnO nanopowder

functionalized with anthocyanins (Fig. 4b). In UV domain, the most intense band is in 330–360 nm wavelength domain, being assigned to the excitonic absorption of ZnO [15, 18]. The position of bands depends on the composition of sample and can be correlated with the particles dimension. The presence of silver is just slightly visible as a shoulder around 400 nm, because the band characteristic to Ag overlaps more intense ones of ZnO. The intensity of shoulder increases from Ag–ZnO **1** to Ag–ZnO **3**, the unexpected low intensity for Ag–ZnO **2** being correlated with the existence of silver in ionic form. In visible domain, an intense absorption from 610 nm, is assigned to anthocyanins in blue form, which are linked to the zinc oxide particles [15, 34]. The spectrum of Ag–ZnO **4** sample is very different, because of the highest quantity of Ag. It can be noticed a continuous absorption in visible domain, with a maximum at 443 nm, in correlation with its dark brown color. Similar shapes of UV–vis spectra were reported for other Ag–ZnO composites with high Ag content [18]. The blue color of Ag–ZnO samples confirmed the presence of anthocyanins bonded in blue form to nanoparticles surface, but the red cabbage aqueous extract contains other organic compounds which can be also involved in the synthesis of Ag nanoparticles, similar with the obtaining in white cabbage extract [1, 10].

The values of band gap energy (E_g) for synthesized nanocomposites were calculated from the UV–vis spectra, using the Tauc equation [35]. The band gap energy for studied ZnO nanoparticles (Fig. 5) can be correlated with particles dimension and their structural characteristics [36]. As it can be seen in Fig. 5, the band gap energy value increases with the Ag content. For all samples, the

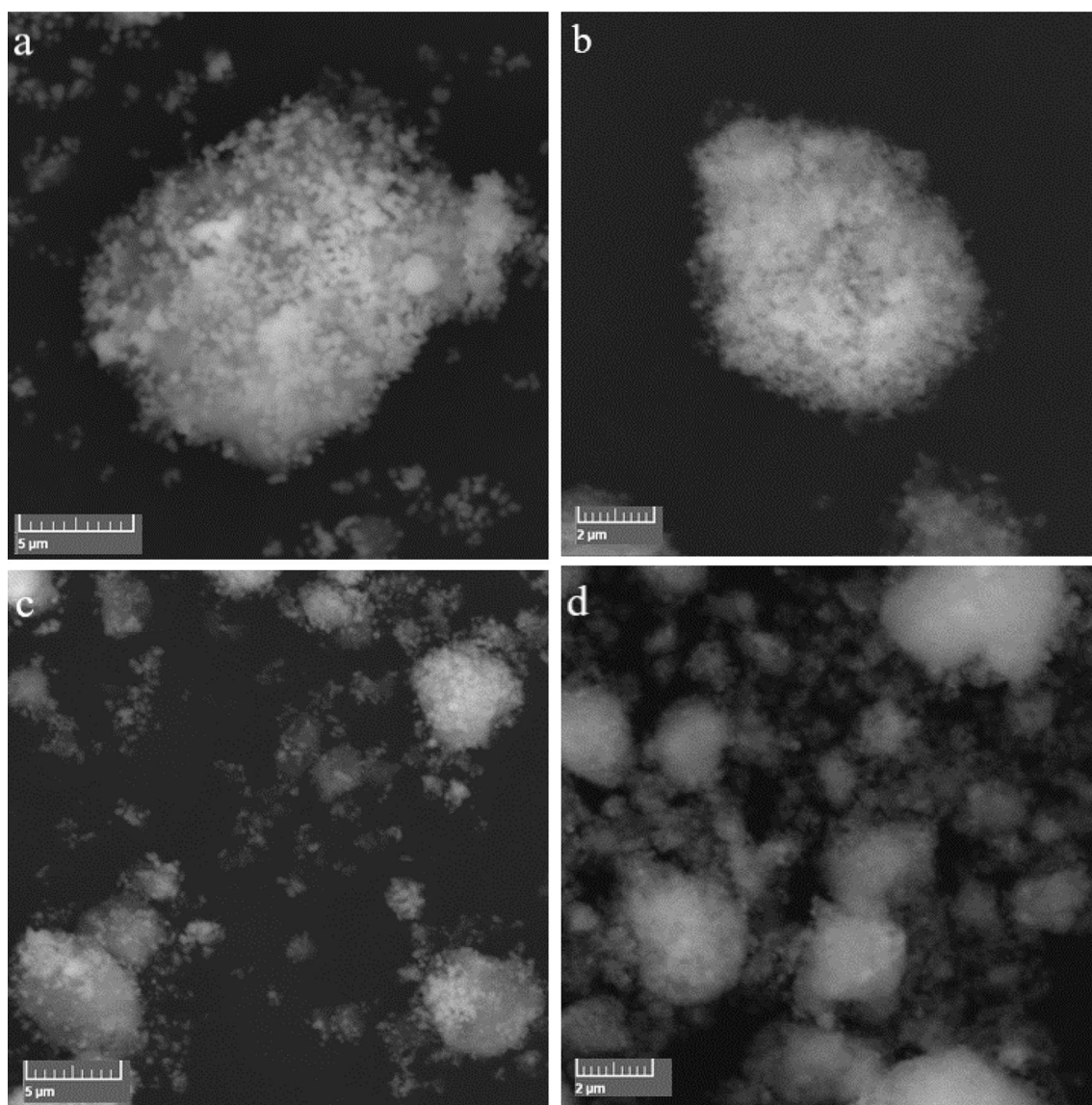


Fig. 2 SEM images for Ag–ZnO powders: **a** Ag–ZnO **1**, **b** Ag–ZnO **2**, **c** Ag–ZnO **3** and **d** Ag–ZnO **4**

Table 1 Ag/Zn molar ratio for Ag–ZnO composites

Samples	Silver:zinc molar ratio
Ag–ZnO 1	1:37
Ag–ZnO 2	1:30
Ag–ZnO 3	1:12
Ag–ZnO 4	1:7

value of E_g is superior to that determined for ZnO nanopowder functionalized with anthocyanins. This variation can be correlated with the decrease of the crystallites dimension with the Ag content, as it was demonstrated by XRD. The TEM images demonstrated a decrease of aggregate dimensions too. This behavior may be considered as an

indirect effect of the functionalization of ZnO with Ag nanoparticles. The irregular value for Ag–ZnO **2** could be explained by the presence of silver as Ag(I).

In the FTIR spectra of Ag–ZnO samples (Fig. 6) very strong bands around 460 cm^{-1} characteristic to ZnO with wurtzite structure can be observed. The profile of bands depends on the shape of ZnO particles, the dielectric constant of the matrix in which material is diluted, and the particles aggregation [37, 38]. For all Ag–ZnO samples, a similar profile of spectra in the $400\text{--}500\text{ cm}^{-1}$ domain can be observed. The different band position is due to the change in the shape and aggregation of ZnO nanoparticles with the silver content, as it was demonstrated by XRD and TEM images.

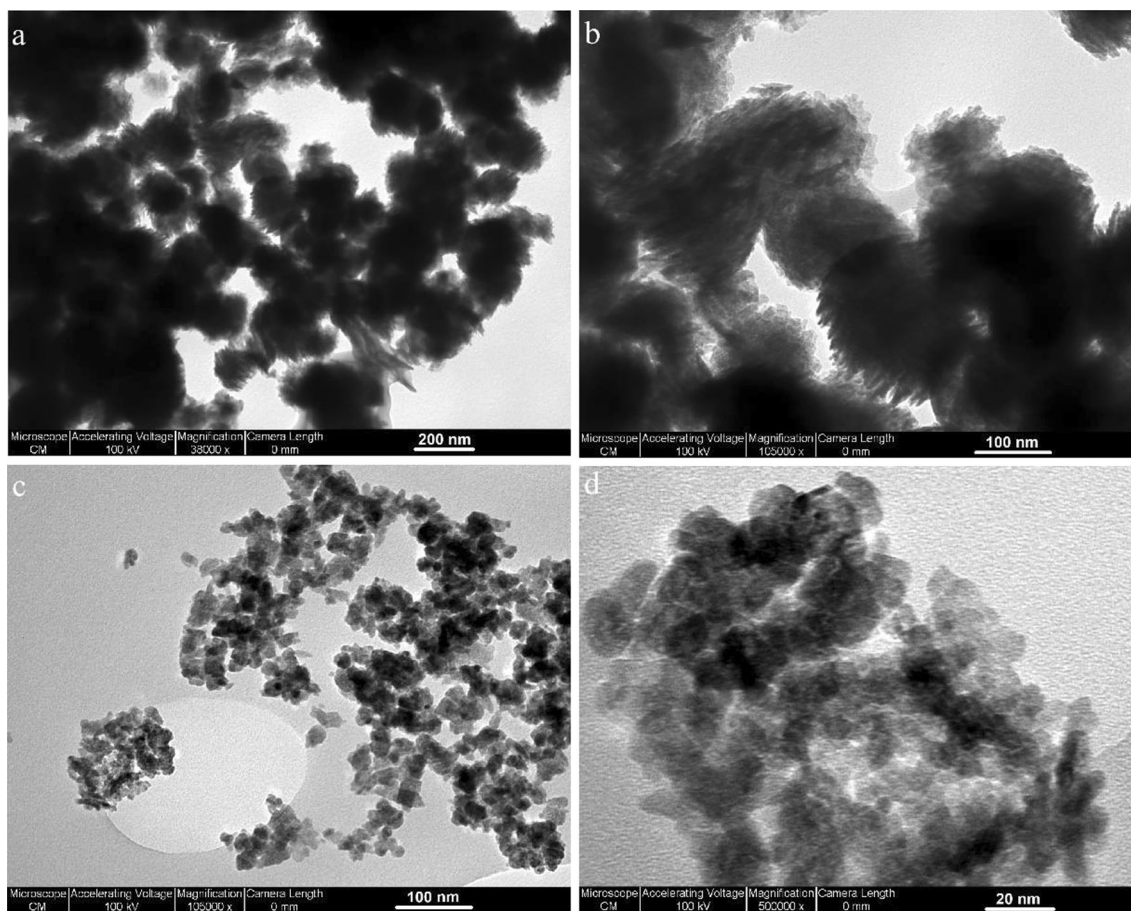


Fig. 3 TEM images for Ag-ZnO 3 (a, b) and Ag-ZnO 4 (c, d) powders, at different magnifications

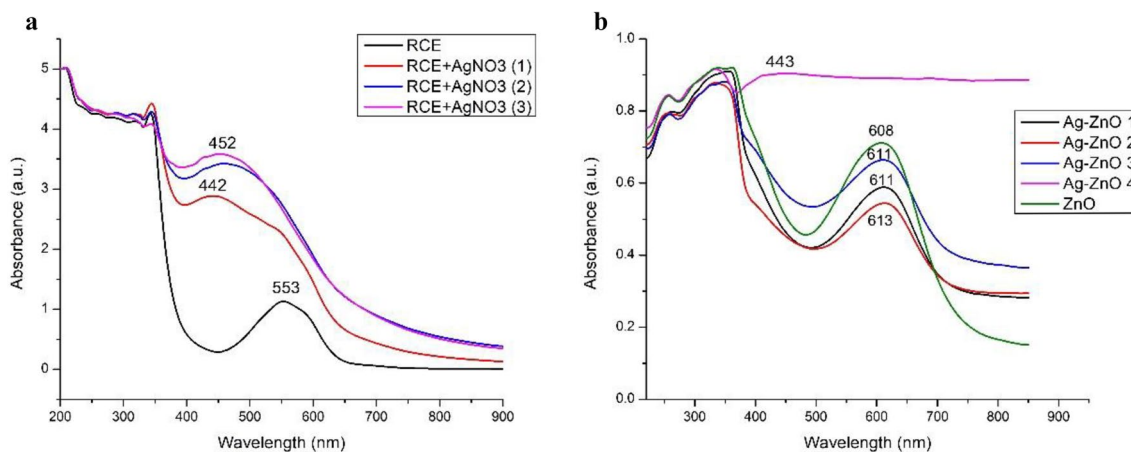


Fig. 4 Color changes of the reagents mixture during the synthesis of Ag nanoparticles, in the first 10 min (a). UV-vis spectra of Ag-ZnO nanocomposites, in comparison with ZnO functionalized with anthocyanins (b) (Color figure online)

The bands assigned to organic compounds are weaker compared with those of ZnO. The most characteristic vibrations attributed to anthocyanins can be found in the wave number range of $1000\text{--}1050\text{ cm}^{-1}$ and $1600\text{--}1650\text{ cm}^{-1}$. In

comparison with the anthocyanin extract [39], the maximum of infrared absorption bands is shifted, probably because of the blue anthocyanins' coordination at the surface of inorganic particles. The bands at 1410 cm^{-1} and 1581 cm^{-1}

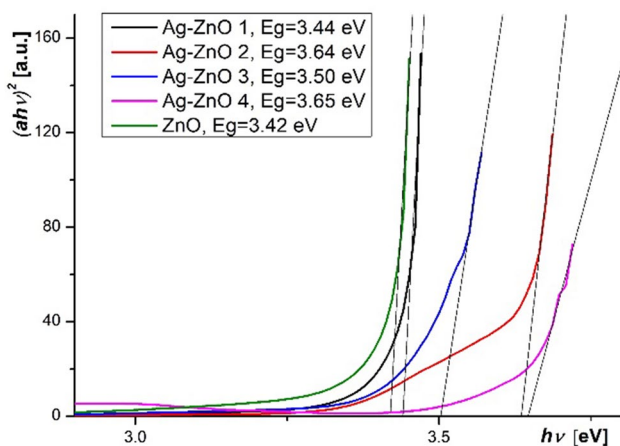


Fig. 5 Tauc plots for Ag–ZnO samples, in comparison with ZnO functionalized with anthocyanins

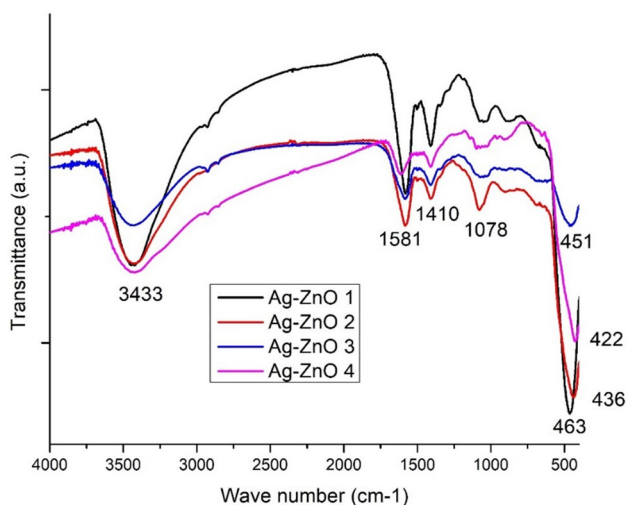


Fig. 6 FTIR spectra of Ag–ZnO samples

can be assigned to residual acetate group ($\nu_{as}COO$ and ν_sCOO), as they were also identified for other zinc binary compounds obtained from zinc acetate precursor [36]. These bands are overlapped with the strong bands assigned to carbonate (found in Ag_2CO_3 spectrum around 1449 cm^{-1} and 1382 cm^{-1} [40]), which explains their different shape, position and intensity. Thus, the band from 1581 cm^{-1} is stronger for Ag–ZnO 1, Ag–ZnO 2, and Ag–ZnO 3, compared to Ag–ZnO 4. Furthermore, in Ag–ZnO 4 the band is shifted to 1610 cm^{-1} . These differences are due to the dissimilar content of Ag_2CO_3 , also identified by XRD in Ag–ZnO 1, Ag–ZnO 2, and Ag–ZnO 3.

The presence of water molecules and hydroxyl groups, which are most probably associated by hydrogen bonding, is evidenced in all spectra by a broad absorption band in the range of $3200\text{--}3600\text{ cm}^{-1}$ [15, 39, 41, 42].

3.2 Antimicrobial Activity

The antibiotic resistance of bacterial strains, fungi and parasites is a current very serious problem to health care and food technology. It was demonstrated that for microbes is difficult to acquire resistance toward nanoparticles as they target multiple bacterial components, contrary to the antibiotics [11]. Besides the advantage of the synergic effect in composite materials, silver containing nanocomposites can provide a slow release of silver ions [3]. The antimicrobial activity of anthocyanins was also highlighted [43]. For these reasons, the Ag-based composite materials can be considered suitable silver carriers.

The antimicrobial activity of Ag–ZnO samples was compared with that of ZnO functionalized with anthocyanins. The differences between prepared composite samples consist in: (i) the size of ZnO crystallites, which decrease from ZnO to Ag–ZnO 4, with the increase of Ag content, (ii) the value of Ag/ZnO ratio—the Ag content increases continuously from Ag–ZnO 1 to Ag–ZnO 4, (iii) the oxidation state of silver—at low concentrations, i.e. in Ag–ZnO 1, Ag–ZnO 2 and Ag–ZnO 3, Ag is present both as Ag(I) and Ag(0), while in Ag–ZnO 4 only metallic silver was identified. All these differences could influence the antimicrobial activity of nanocomposites.

The antibacterial activity of ZnO nanoparticles was explained by other authors [44] based on a reaction of ZnO surface with water. In the aqueous suspensions of small nanoparticles of ZnO are produced higher levels of hydroxyl radicals. The antibacterial effect of ZnO nanoparticles was demonstrated on species as *E. coli* (Gram negative) and *Staphylococcus aureus* (Gram positive), and correlated with small size and corresponding large specific surface area for ZnO nanoparticles. The effects are size dependent and do not exist in the range of microscale particles [44]. Due to their high surface area, the Ag nanoparticles can easily generate Ag(I) ions [3], which improves the antibacterial activity of ZnO nanoparticles.

The width of inhibition zone recorded by disk diffusion tests (Table 2) indicates a moderate to good activity of anthocyanins functionalized ZnO nanopowder and Ag–ZnO nanocomposites. The response of individual microbial species is variable and distinct. Thus, most sensitive strains were *S. aureus* and *Streptococcus* for which it was recorded the largest width of inhibition zone, ranging from 6 to 9 mm. *E. coli* and *Candida* sp. displayed an intermediate response (between 2 mm and 4 mm width of growth inhibition zone), while *Pseudomonas* strains were most resistant showing narrow inhibition zone of only 2 mm width. The values for MIC (Table 3) are in $10\text{ }\mu\text{g/mL}$ (*Streptococcus* sp.)— $160\text{ }\mu\text{g/L}$ (*Pseudomonas*, *E. coli*) range.

The anthocyanins functionalized ZnO nanopowder has a moderate to good antimicrobial activity, most sensitive

Table 2 Antimicrobial activity for Ag–ZnO functionalized with anthocyanins nanocomposites, in comparison with ZnO functionalized with anthocyanins against various clinical isolated strains

Strains	Width of growth inhibition zone (mm)				
	Ag–ZnO 1	Ag–ZnO 2	Ag–ZnO 3	Ag–ZnO 4	ZnO
<i>Staphylococcus aureus</i>	8	9	9	9	8
<i>Streptococcus</i>	7	7	7	7	6
<i>E. coli</i>	3	3	3	3	3
<i>Pseudomonas</i>	2	2	2	2	2
<i>Candida</i>	3	3	4	4	3

Table 3 Minimal inhibitory concentration for Ag–ZnO composites in comparison with ZnO functionalized with anthocyanins

Strains	MIC ($\mu\text{g/mL}$)				
	Ag–ZnO 1	Ag–ZnO 2	Ag–ZnO 3	Ag–ZnO 4	ZnO
<i>Staphylococcus</i>	40	40	20	20	40
<i>Streptococcus</i>	20	20	20	10	20
<i>E. coli</i>	160	160	160	80	160
<i>Pseudomonas</i>	160	160	160	160	160
<i>Candida</i>	80	80	80	80	160

bacteria being once again *Streptococcus* and *Staphylococcus*. The antifungal activity of ZnO functionalized with anthocyanins is comparable or superior to other ZnO nanoparticles obtained in vegetal extracts [45]. By further functionalization of ZnO with Ag nanoparticles, an increase of antimicrobial activity would be expected, both because of lower ZnO crystallites size and the effect of Ag nanoparticles. Based on inhibition zone width and MIC value, the increase of antimicrobial activity with the Ag content can be noticed for *Staphylococcus*, *Streptococcus*, *E. coli* and *Candida*, but the variation is low. Against *Staphylococcus*, the decrease of MIC value was noticed to a lower Ag concentration compared to *Streptococcus* and *E. coli*. The highest antimicrobial activity was determined for Ag–ZnO 4 sample. No variation with Ag content was noticed against *Pseudomonas*.

This behavior can be explained based on the composites structure. The Ag nanoparticles are covered by ZnO, forming aggregates, as it was demonstrated by SEM and TEM investigation (Figs. 2, 3). The growth of aggregates and the localization of Ag nanoparticles inside of them lead to a slower silver ion release, which is probably responsible for no or small variation of antimicrobial activity. However, the morphology can increase the storage and the release time for Ag. As well, the bacterial resistance to toxic metals was reported, but the molecular mechanisms behind the silver resistance are still not completely understood [3].

For comparison, other reported MIC values for Ag–ZnO nanocomposites are 600 $\mu\text{g/mL}$ and 400 $\mu\text{g/mL}$ against *E. coli* and *S. aureus* [46], or 550 $\mu\text{g/mL}$ and 60 $\mu\text{g/mL}$ for a Ag–ZnO nanocomposite with nearly equimolar Zn/Ag ratio (1:0.88) [11]. Thus, although the deposition onto Ag nanoparticles did not significantly increase the antimicrobial activity of ZnO functionalized with anthocyanins, a good antimicrobial activity can be assigned to synthesized nanocomposite samples, probably due to anthocyanins, too.

We started from a very low content of Ag in Ag–ZnO composites to demonstrate the silver influence, i.e. even a very small amount of Ag in nanocomposite is enough to increase the antimicrobial activity against *Staphylococcus* and *Candida*.

3.3 Photocatalytic Properties

It is well known that pure and doped zinc oxide, and also composite materials containing ZnO are efficient photocatalysts, widely used in a variety of photocatalytic processes [47]. The functionalization of ZnO particles with both anthocyanins and Ag could increase the PA, such as the materials absorb in the visible region of the solar spectrum, not only in the UV. The functionalization of ZnO with anthocyanins by one-pot method demonstrated this assumption [15].

It was measured the absorbance at 497 nm of CR solutions during the photocatalytic experiments as a function of irradiation time. The PA of ZnO nanopowders was estimated through the C_t/C_0 ratio (Fig. 7a) for a rate of 0.05 g catalyst/100 mL CR solution 30 mg/L. The results demonstrated a slight increase of PA with the silver content, but only for low Ag concentration up to Ag/Zn molar ratio of 1:12 (Ag–ZnO 1, Ag–ZnO 2, Ag–ZnO 3). An abrupt decrease of PA was identified for the sample with highest silver content (Ag–ZnO 4). For example, after 120 min the values of PA were: 88.39% (Ag–ZnO 3), 86.57% (Ag–ZnO 2), 84.52% (Ag–ZnO 1), and 67.46% (Ag–ZnO 4). The highest value (for Ag–ZnO 3) is similar to that previously reported for ZnO functionalized with anthocyanins (88.1% [15]), but for lower Ag/ZnO molar ratio than 1/12 the PA is slightly inferior compared to ZnO functionalized with anthocyanins. However, the variations are not high. The decomposition of CR in addition to the azo bond breaking

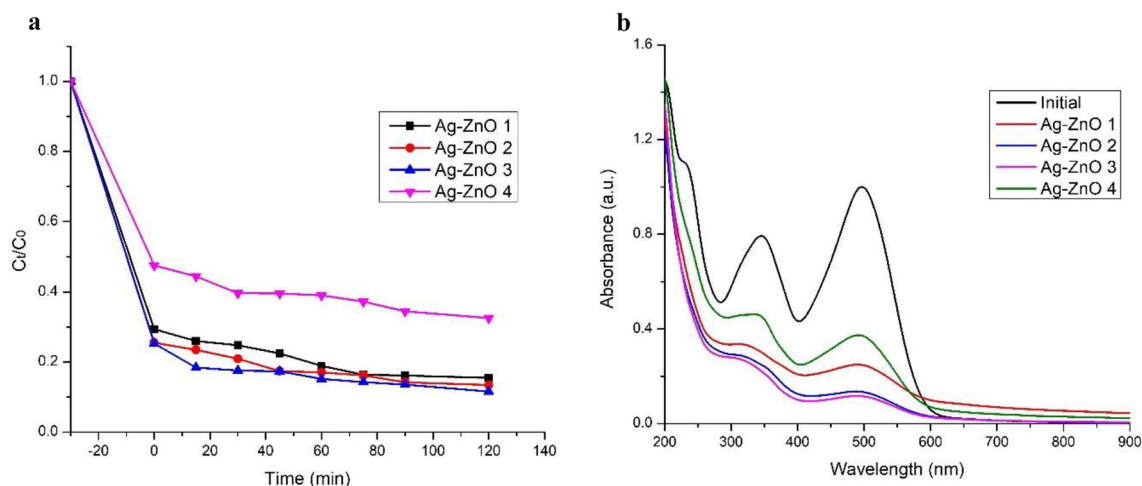


Fig. 7 Photodegradation of CR by Ag–ZnO nanocomposites functionalized with anthocyanins, with various Ag content (**a**). UV–vis spectra of CR solutions before and after photodegradation (120 min) onto Ag–ZnO nanocomposites (**b**)

is demonstrated by the modification of electronic spectra of CR solutions in UV domain (Fig. 7b).

The variation of PA with the Ag content for pristine Ag–ZnO nanocomposites was reported in other studies. Zhang and Mu found that the degradation rate increases with the silver content increase up to a content level of 6.2% and then decreases with further increase of Ag content in Ag–ZnO, the optimum Ag amount being approximately 6.2% [48]. Liu et al. found a similar value (6% Ag) for ZnO rods decorated with Ag nanoparticles in photocatalytic degradation of methylene blue [49]. Other authors demonstrated that the PA of Ag-doped ZnO samples first increases with the Ag content up to 1%, and then slightly decreases with further Ag doping (2% and 4%) [50]. If the general behavior of Ag–ZnO composites is accepted by several authors, the concentration of Ag, which influences the photocatalytic properties depends on other composite properties and/or synthesis routes. Zhang and Mu [48] considered that the improvement of Ag–ZnO materials photoactivity can be explained by better charge separation in the case of Ag–ZnO composites in comparison with pristine ZnO, but the incorporation of Ag onto the ZnO surface can increase the rate of electron transfer to the dissolved oxygen. At higher Ag concentration, silver particles can act as recombination centers, which is caused by the electrostatic attraction of negatively charged silver and positively charged holes [48]. In consequence, a proper content of silver can reduce electron–hole recombination and increase the PA.

The bleaching of the CR solution in the presence of photocatalyst, in dark, is an evidence for the adsorption capacity of ZnO powders. The synthesized Ag–ZnO nanocomposites demonstrated high adsorption capacity, probably because of a high surface area. In the absence of catalyst, an irrelevant

variation of CR concentration was identified [26], which indicates the dye high stability.

The values of PA for composite materials with low Ag content are higher, but comparable with those obtained for pristine ZnO produced by precipitation (86.4% after 2 h [15]) and superior to ZnO capped with anthocyanins (67.46% after 2 h). Pristine ZnO obtained by thermal decomposition of anthocyanins functionalized ZnO have a lower PA because of larger particles [42]. The compared values are determined in similar conditions, because a comparison between PA values involves analogous experimental conditions, like the dye/catalyst ratio and time of photocatalytic experiment.

It was used the widely accepted kinetic mechanism Langmuir–Hinshelwood (L–H) model in the study of CR degradation over Ag–ZnO nanocomposites. L–H model considers all processes involved in a heterogenous catalysis, including the adsorption of substrate onto the photocatalyst surface. The model considers the reactant more strongly adsorbed on the catalyst surface than the products, and consequently the rate of unimolecular surface reaction is proportional to the surface coverage [51–53]

The L–H simplified equation [54] can be written in a linearized form:

$$\ln Q = \ln Q_0 - k_{app} \cdot t, \quad (2)$$

where Q is the concentration of the reactant (mg/L), Q_0 is the initial value of the reactant concentration and t is the illumination time. A linear fit of the plot of $\ln Q$ against time was performed, thus the slope and the intercept of trend line give the values of k_{app} and Q_0 , respectively. The results are shown in Table 4.

The small differences between Q_0 and $Q_{0,exp.}$ and good values of R^2 demonstrated that the kinetics of the

Table 4 Kinetic parameters (reaction rate, k_{app} ; experimental and calculated value of CR concentration after dark adsorption, Q_0 ; coefficient of determination, R^2) for the photocatalytic degradation of CR dye with Ag–ZnO nanocomposites as catalysts (0–120 min)

Samples	$Q_{0,exp}$ (mg/L)	L–H simplified model		
		Q_0 (mg/L)	k_{app} (min^{-1})	R^2
Ag–ZnO 1	6.94	6.73	0.0061	0.932
Ag–ZnO 2	6.02	5.79	0.0058	0.951
Ag–ZnO 3	5.95	5.19	0.0058	0.916
Ag–ZnO 4	11.35	10.96	0.0031	0.945

photocatalytic process is a L–H-type. The values of $Q_{0,exp}$, hence the dye concentration after the adsorption in dark, denotes the adsorption capacity of nanocomposites. Thus, the adsorption capacity and the decomposition rate increase with the Ag content at low concentrations (Ag–ZnO 1–Ag–ZnO 3), but for higher Ag concentration both adsorption capacity and reaction rate decrease (Ag–ZnO 4).

4 Conclusion

New Ag–ZnO nanocomposites with different Ag/Zn molar ratio were obtained in anthocyanins extract. The TEM investigation demonstrated that ZnO was deposited onto Ag nanoparticles resulting larger aggregates. In the case of composites with low silver content (up to 1/12 Ag/Zn) both Ag(0) and Ag(I) as Ag_2CO_3 were found. The decrease of ZnO crystallites size with the Ag content increase is noticeable. During the synthesis of Ag nanoparticles, the surface plasmon band centered around 450 nm characteristic to silver nanoparticles was identified, but in composite nanomaterials the band is overlapped, being clearly identified only for the highest silver concentration (Ag/ZnO molar ratio of 1/7). The band gap energy values are in the range of 3.44–3.65 eV, superior to that of ZnO functionalized with anthocyanins. Despite of low Ag/ZnO molar ratios, the synergic effect of antimicrobial activity against *Staphylococcus*, *Streptococcus*, *E. coli* and *Candida* was demonstrated. Small differences in PA were observed in the degradation of CR azo dye for low Ag content in nanocomposites, which have a high efficiency (PA = 81–85% after 60 min), while a decrease of photoactivity was noted at high Ag content, Ag/ZnO = 1/7 (PA = 61% after 60 min). Having in view both antimicrobial and photocatalytic properties, the obtained Ag–ZnO nanocomposites functionalized with anthocyanins are proper materials for the treatment of water, being able to prevent contamination and spreading of microorganisms in different applications.

Compliance with Ethical Standards

Conflict of interest The authors declare no conflict of interest regarding this study.

References

1. A. Singh, B. Sharma, R. Deswal, J. Trace Elem. Med. Biol. **47**, 1 (2018). <https://doi.org/10.1016/j.jtemb.2018.01.001>
2. J.K. Patra, K.H. Baek, J. Nanomater. **2014**, 417305 (2014). <https://doi.org/10.1155/2014/417305>
3. S. Eckhardt, P.S. Brunetto, J. Gagnon, M. Priebe, B. Giese, K.M. Fromm, Chem. Rev. **113**, 4708 (2013). <https://doi.org/10.1021/cr300288v>
4. L. David, B. Moldovan, A. Vulcu, L. Olenic, M. Perde-Schrepler, E. Fischer-Fodor, A. Florea, M. Crisan, I. Chiorean, S. Clitic, G.A. Filip, Colloid Surf. B **122**, 767 (2014). <https://doi.org/10.1016/j.colsurfb.2014.08.018>
5. A.S. Ethiraj, S. Jayanthi, C. Ramalingam, C. Banerjee, Mater. Lett. **185**, 526 (2016). <https://doi.org/10.1016/j.matlet.2016.07.114>
6. C. Dong, X. Zhang, H. Cai, C. Cao, Optik **127**, 10378 (2016). <https://doi.org/10.1016/j.ijleo.2016.08.055>
7. U.B. Jagtap, V.A. Bapat, Ind. Crop Prod. **46**, 132 (2013). <https://doi.org/10.1016/j.indcrop.2013.01.019>
8. N. Abdel-Raouf, R.M. Alharbi, N.M. Al-Enazi, M.M. Alkhulaifi, I.B.M. Ibraheem, Beni-Suef Univ. J. Basic Appl. Sci. **7**, 150 (2018). <https://doi.org/10.1016/j.bjbas.2017.10.003>
9. P. Kuppusamy, S.J.A. Ichwan, N.R. Parine, M.M. Yusoff, G.P. Maniam, N. Govindan, J. Environ. Sci. **29**, 151 (2015). <https://doi.org/10.1016/j.jes.2014.06.050>
10. R. Tamileswari, M. Haniff Nisha, S.S. Jesurani, Int. J. Eng. Res. Technol. **4**, 1071 (2015)
11. I. Matai, A. Sachdev, P. Dubey, S.U. Kumar, B. Bhushan, P. Gopinath, Colloid Surf. B **115**, 359 (2014). <https://doi.org/10.1016/j.colsurfb.2013.12.005>
12. C. Ray, T. Pal, J. Mater. Chem. A **5**, 9465 (2017). <https://doi.org/10.1039/C7TA02116J>
13. S. Ahmed, S.A. Annu Chaudhry, S. Ikram, J. Photochem. Photobiol. B **166**, 272 (2017). <https://doi.org/10.1016/j.jphotobiol.2016.12.011>
14. H. Agarwal, S.V. Kumar, S. Rajeshkumar, Resour. Effic. Technol. **3**, 406 (2017). <https://doi.org/10.1016/j.refitt.2017.03.002>
15. A. Dumbrava, D. Berger, G. Prodan, C. Matei, F. Moscalu, A. Diacon, ECS J. Solid State Sci. Technol. **6**, P870 (2017). <https://doi.org/10.1149/2.0311712jsss>
16. H.A. Oualid, Y. Essamlali, O. Amadine, K. Daanoun, M. Zahouily, Ceram. Int. **43**, 13786 (2017). <https://doi.org/10.1016/j.ceramint.2017.07.097>
17. S.T. Kochuveedu, Y.H. Jang, D.H. Kim, Chem. Soc. Rev. **42**, 8467 (2013). <https://doi.org/10.1039/c3cs60043b>
18. S. Rajaboopathi, S. Thambidurai, J. Mol. Liq. **262**, 148 (2018). <https://doi.org/10.1016/j.molliq.2018.04.073>
19. S. Rajaboopathi, S. Thambidurai, Mater. Chem. Phys. **223**, 512 (2019). <https://doi.org/10.1016/j.matchemphys.2018.11.034>
20. S. Ghosh, V.S. Goudar, K.G. Padmalekha, S.V. Bhat, S.S. Indi, H.N. Vasan, RSC Adv. **2**, 930 (2012). <https://doi.org/10.1039/c1ra00815c>
21. A.B.P. Jimenez, C.A.H. Aguilar, J.M.V. Ramos, P. Thangarasu, Aust. J. Chem. **68**, 288 (2015). <https://doi.org/10.1071/CH14123>
22. J.H. Ortez, Disk diffusion testing, in *Manual of Antimicrobial Susceptibility Testing*, coord. ed. by M.B. Coyle (American Society for Microbiology, 2005)

23. National Committee for Clinical Laboratory Standards, *Methods for Determining Bactericidal Activity of Antimicrobial Agents. Approved Guideline M26-A* (National Committee for Clinical Laboratory Standards, Wayne, 1999)
24. National Committee for Clinical Laboratory Standards, *Performance Standards for Antimicrobial Disk Susceptibility Tests. Approved Standard M2-A8*, 8th edn. (National Committee for Clinical Laboratory Standards, Wayne, 2003)
25. D.R. Pearson, R.T. Steigbigel, H.T. Davis, *Antimicrob. Agents Chemother.* **8**, 699 (1980)
26. A. Dumbrava, D. Berger, G. Prodan, F. Moscalu, A. Diacon, *Mater. Chem. Phys.* **173**, 70 (2016). <https://doi.org/10.1016/j.matchemphys.2016.01.040>
27. A. Dumbrava, G. Prodan, D. Berger, M. Bica, *Powder Technol.* **270**, 197 (2015). <https://doi.org/10.1016/j.powtec.2014.10.012>
28. Y.T. Prabhu, K.V. Rao, V.S.S. Kumar, B.S. Kumari, *World J. Nano Sci. Eng.* **4**, 21 (2014). <https://doi.org/10.4236/wjnse.2014.41004>
29. K. Omri, A. Alyamani, L. El Mir, *Appl. Phys. A* **124**, 215 (2018). <https://doi.org/10.1007/s00339-018-1657-7>
30. S. Kamyar, M. Bin Ahmad, E.A.J. Al-Mulla, N.A. Ibrahim, P. Shabanzadeh, A. Rustaiyan, Y. Abdollahi, S. Bagheri, S. Abdolmohammadi, M.S. Usman, M. Zidan, *Molecules* **17**, 8506 (2012). <https://doi.org/10.3390/molecules17078506>
31. S. Baker, M.N. Nagendra Prasad, B.L. Dhananjaya, K. Mohan Kumar, S. Yallappa, S. Satish, *Enzyme Microb. Technol.* **95**, 128 (2016). <https://doi.org/10.1016/j.enzmictec.2016.10.004>
32. R. Desai, V. Mankad, S.K. Gupta, P.K. Jha, *Nanosci. Nanotechnol. Lett.* **4**, 30 (2012). <https://doi.org/10.1166/nnl.2012.1278>
33. Z. Zaheer, Rafiuddin, *Colloid Surf. B* **90**, 48 (2012). <https://doi.org/10.1016/j.colsurfb.2011.09.037>
34. H.E. Khoo, K.N. Prasad, K.W. Kong, Y. Jiang, A. Ismail, *Molecules* **16**, 1710 (2011). <https://doi.org/10.3390/molecules16021710>
35. J. Tauc, R. Grigorovici, A. Vancu, *Phys. Status Solidi B* **15**, 627 (1966). <https://doi.org/10.1002/pssb.19660150224>
36. A. Dumbrava, D. Berger, G. Prodan, F. Moscalu, A. Diacon, *Z. Phys. Chem.* **232**, 61 (2017). <https://doi.org/10.1515/zpch-2017-0005>
37. A. Šarić, S. Musić, M. Ivanda, *J. Mol. Struct.* **993**, 219 (2011). <https://doi.org/10.1016/j.molstruc.2010.10.018>
38. A. Dumbrava, G. Prodan, F. Moscalu, *Mater. Sci. Semicond. Process.* **16**, 1095 (2013). <https://doi.org/10.1016/j.mssp.2013.03.007>
39. V.A. Pereira Jr., I.N.Q. de Arruda, R. Stefani, *Food Hydrocoll.* **43**, 180 (2015). <https://doi.org/10.1016/j.foodhyd.2014.05.014>
40. Y. Song, J. Zhu, H. Xu, C. Wang, Y. Xu, H. Ji, K. Wang, Q. Zhang, H. Li, *J. Alloy Compd* **592**, 258 (2014). <https://doi.org/10.1016/j.jallcom.2013.12.228>
41. J. Coates, Interpretation of infrared spectra. A practical approach, in *Encyclopedia of Analytical Chemistry*, ed. by R.A. Meyers (Wiley, Chichester, 2000)
42. A. Dumbrava, D. Berger, G. Prodan, M. Badea, R. Olar, F. Moscalu, A. Diacon, *Appl. Phys. A* **124**, 819 (2018). <https://doi.org/10.1007/s00339-018-2227-8>
43. A. Cisowska, D. Wojnicz, A.B. Hendrich, *Nat. Prod. Commun.* **6**, 149 (2011)
44. G. Applerot, A. Lipovsky, R. Dror, N. Perkas, Y. Nitzan, R. Lubart, A. Gedanken, *Adv. Funct. Mater.* **19**, 842 (2009). <https://doi.org/10.1002/adfm.200801081>
45. P. Jamdagni, P. Khatri, J.S. Rana, *J. King Saud Univ. Sci.* **30**, 168 (2018). <https://doi.org/10.1016/j.jksus.2016.10.002>
46. W. Lu, G. Liu, S. Gao, S. Xing, J. Wang, *Nanotechnology* **19**, 445711 (2008). <https://doi.org/10.1088/0957-4484/19/44/445711>
47. K. Omri, N. Alonizan, *J. Inorg. Organomet. Polym.* **29**, 203 (2019). <https://doi.org/10.1007/s10904-018-0979-4>
48. Y. Zhang, J. Mu, *J. Colloid Interface Sci.* **309**, 478 (2007). <https://doi.org/10.1016/j.jcis.2007.01.011>
49. H. Liu, L. Zhong, S. Govindaraju, K. Yun, *J. Phys. Chem. Solids* **129**, 46 (2019). <https://doi.org/10.1016/j.jpcs.2018.12.040>
50. O. Bechambi, M. Chalbi, W. Najjar, S. Sayadi, *Appl. Surf. Sci.* **347**, 414 (2015). <https://doi.org/10.1016/j.apsusc.2015.03.049>
51. B. Liu, X. Zhao, C. Terashima, A. Fujishima, K. Nakata, *Phys. Chem. Chem. Phys.* **16**, 8751 (2014). <https://doi.org/10.1039/c3cp55317e>
52. M.A. Behnajady, N. Modirshahla, R. Hamzavi, *J. Hazard. Mater.* **133**, 226 (2006). <https://doi.org/10.1016/j.jhazmat.2005.10.022>
53. A. Nageswara Rao, B. Sivasankar, V. Sadasivam, *J. Hazard. Mater.* **166**, 1357 (2009). <https://doi.org/10.1016/j.jhazmat.2008.12.051>
54. I.K. Konstantinou, T.A. Albanis, *Appl. Catal. B* **42**, 319 (2003). [https://doi.org/10.1016/S0926-3373\(02\)00266-7](https://doi.org/10.1016/S0926-3373(02)00266-7)

Publisher's Note Springer Nature remains neutral with regard to jurisdictional claims in published maps and institutional affiliations.